



Contents lists available at [ScienceDirect](https://www.sciencedirect.com)

Power Electronic Devices and Components

journal homepage: www.journals.elsevier.com/power-electronic-devices-and-components



Modelling the fatigue damage in power components using machine learning technology

Stoyan Stoyanov^{a,*}, Razia Sulthana^a, Tim Tilford^a, Xiaotian Zhang^b, Yihua Hu^c, Xingyu Yang^d, Yaochun Shen^d, Yangang Wang^e

^a School of Computing and Mathematical Sciences, University of Greenwich, London, UK

^b Department of Electronic Engineering, University of York, York, UK

^c Engineering, Faculty of Natural, Mathematical & Engineering Sciences, King's College London, London, UK

^d Department of Electrical Engineering and Electronics, University of Liverpool, Liverpool, UK

^e Dynex Semiconductor Ltd, Lincoln, UK

ARTICLE INFO

Keywords:

Power components
Power electronics module
IGBT
Wire bonds
Thermal fatigue
Damage
Reliability
Machine Learning
Neural network
Physics-informed data

ABSTRACT

Thermo-mechanical finite element (FE)-based simulation technology has been used extensively for virtual prototyping and to predict material degradation and thermal fatigue damage in electronics assembly materials. However, from an end-user point of view, the deployment of such high-fidelity modelling is not straightforward as it requires comprehensive device and material characterisation data that is not readily available through technical datasheets and must be gathered using costly and time-consuming bespoke characterisation tests and access to metrology instruments. In addition to that, FE modelling requires access to advanced software and specialised FE skill sets. Here, a novel physics-informed Machine Learning (ML) approach for developing computationally fast metamodels for predicting fatigue damage and its spatial distribution at common failure sites of power electronics components is developed, validated and demonstrated. The significance of this work is in the attributes and the capabilities of the proposed modelling technology that enable the end-users of power components to perform insightful model-based assessments of the thermal fatigue damage in the assembly materials due to different application-specific, qualification and user-defined load conditions, removing current requirements for comprehensive device characterisations and deploying complex finite element models. The proposed methodology is demonstrated with two different metamodel structures, a regression decision tree and a neural network, for the problem of predicting the thermal fatigue damage in wire bonds of insulated-gate bipolar transistor (IGBT) power electronics modules (PEMs) exposed to passive temperature cycling loads. The results confirmed that the proposed approach and the modelling technology could offer FE model substitution and the capability to spatially map highly nonlinear three-dimensional spatial distributions of the damage parameter over local sub-domains associated with material fatigue degradation and failure.

1. Introduction

Assuring and assessing the reliability performance of power electronics modules (PEMs) deployed in different applications remains a key challenge for the industry (Falck et al., 2018; Wang & Blaabjerg, 2021; Yang et al., 2020; Gonzalez et al., 2016). Based on current packaging architectures, power components are most susceptible to thermally induced fatigue damage of their wire bonds and the die attachment layer. While many studies contributed to the design-for-reliability and reliability assessment modelling of PEMs (Li et al., 2023; Huang et al.,

2021; Rajaguru, Lu & Bailey, 2019; Dudek et al., 2020; Shishido et al., 2019; Gabriel & Huitink, 2023; Ma, Wang & Blaabjerg, 2016), the informed deployment of these modules in different applications remains challenging for the end users. Driven by considerations for protecting their Intellectual Property (IP), information and data on internal layout, topology and geometric dimensions of power components and their bill of materials are not included in manufacturers' technical datasheets and thus are not readily available. To evaluate or assure the required reliability of PEMs under application-specific load conditions, the end-users must engage in time-consuming and costly activities to characterise the

* Corresponding author.

E-mail address: s.stoyanov@gre.ac.uk (S. Stoyanov).

<https://doi.org/10.1016/j.pedc.2025.100079>

Received 10 November 2024; Received in revised form 20 December 2024; Accepted 8 January 2025

Available online 9 January 2025

2772-3704/© 2025 The Authors. Published by Elsevier Ltd. This is an open access article under the CC BY license (<http://creativecommons.org/licenses/by/4.0/>).

component and to assess its reliability performance through simulation and/or physical testing.

Finite element (FE) modelling, coupled with lifetime prediction methodologies and models, offers a robust solution for this problem by predicting damage metrics for the expected failure modes, for example, the studies reported in Rajaguru, Lu and Bailey (2019), Dudek et al. (2020), Shishido et al. (2019), Grams et al. (2014). Lifetime prediction methodologies for PEM have also been extensively developed, with much of the effort on establishing accurate models predicting the wire bonds lifetime under accelerated active and passive temperature cycling conditions that qualify the device for the respective application load. Most commonly, lifetime models such as Coffin-Manson and Paris laws require damage parameter values that are semi-empirically correlated to the cycles to failure. A damage metric is often obtained with FE simulation for the failure of wire bonds and solder interconnections in PEMs. Such a lifetime modelling approach has been demonstrated extensively, for example in the studies Rajaguru, Lu and Bailey (2019), Grams et al. (2014), Busca et al. (2011). However, developing and using such FE-based computational models to predict damage, and then lifetime, are complex tasks requiring characterisation data, specialist skills, computing hardware, and advanced simulation software tools unavailable to many end-users.

One of the main limitations of most of the published modelling work on thermal fatigue failure of wire bonds in power electronic modules is the simplified assumptions for their material behaviour. Important considerations such as temperature-dependent plastic and particularly creep characteristics are often not included. The creep behaviour of wire interconnects in power modules is rarely considered but test data suggest it is an important element of the mechanistic response of aluminium wires (Yang, Agyakwa & Johnson, 2014; Shishido et al., 2021). However, material constitutive equations of the inelastic behaviour of aluminium wires, most used as interconnects in power components, are rarely available. As a result, creep responses are commonly ignored in FEA studies of power modules.

In this work, the authors address the above position, and the challenges related to that, by advancing their previous work for developing fast, compact, and user-friendly damage prediction models using multi-quadratic interpolation metamodelling (Stoyanov, Tilford, Shen, & Hu, 2024) into machine learning (ML) modelling methodology. It takes advantage of the combined deployment of accurate material models and physics-informed damage data with a three-dimensional spatial location label. The damage datasets are synthetically generated using high-fidelity thermo-mechanical simulations. Unlike non-linear response surface methodology-based studies (Tauscher et al., 2023; Rajaguru, Stoyanov, Lu & Bailey, 2013; Ji et al., 2015) and relatively complex numerical algorithms for model order reduction of full-scale finite element models (Hassan et al., 2024), the proposed approach features simplicity and improved accuracy. A novel attribute is associated with an enhanced level of fidelity that enables, thanks to the deployment of machine learning, the prediction and visualisation of the damage parameter spatial distribution at the local failure site of interest in the power component. The proposed use of ML models protects the manufacturer's intellectual property because they do not require any information about the packaging design, the internal component layout and topology, and the bill of materials. At the same time, they can be deployed by end-users of power devices with ease, to allow assessing the damage under user-defined application loads and visualise the damage distribution. This would allow for the informed deployment of power electronics components across different applications through a better understanding of their reliability performance under respective load conditions.

2. Methodology

The proposed modelling methodology features several key attributes. Firstly, this is the synthetic generation of physics-informed

datasets for the predicted damage parameter using results from high-fidelity non-linear finite element thermal-mechanical simulation. These synthetic data are required to construct and validate the proposed machine-learning model structures. Secondly, the complete automation of the steps associated with the batch setup of the finite element models and load cases, the simulation runs of these scenarios, and the processing of the damage parameter predictions are also critical attributes of the reported computational approach that are required to make it feasible and practical from an implementation point of view.

First, a fully scripted high-fidelity parametric finite element model generation and design-of-simulations based on several load-case setups and analysis runs are carried out for the PEM structure of interest. The models are designed to enable assessing the damage level at anticipated failure sites in the power component (e.g. in wire bonds, solder attachment layer, etc.) as a function of user-defined temperature cyclic loads. The proposed methodology utilises a series of high-fidelity analyses in the thermal load design space which allow for generating physics-informed synthetic data that embeds the relationship between the load condition and the damage spatial distribution across the failure site of interest. These labelled datasets are then deployed in the regression machine learning of the selected model structures such as those demonstrated in this work Neural Network and Decision Tree models. The models are computationally fast metamodelling that can provide predictions not only for a single representative damage characteristic value associated with the failure mode and failure site (e.g. wire bond cracking and wire liftoff) but also a much more detailed and insightful prediction for the spatial distribution of the damage parameter across the failure site. The latter is a very important and novel attribute of the proposed modelling approach as it enables a robust deployment of different lifetime models in the public domain that may have different definitions of the required lifetime model input value of the damage metric. Such damage metrics are often obtained through a location-dependent or a spatial sub-domain-dependent calculation (e.g. volume-weighted average) using the respective damage parameter values in that spatial domain.

The methodology steps are visually outlined with the block diagram given in Fig. 1 and involve the following:

- **Component Characterisation Data.** The power component of interest is fully characterised in terms of internal structure, geometric dimensions, bill of materials and material properties and their non-linear behaviour. As we envisage the methodology to be used by power electronics manufacturers, who can deliver ML models to end-users without disclosing IP, the component characterisation data will be typically readily available. A critical sub-step is the derivation or deployment, if readily available, of accurate material constitutive laws for the non-linear material behaviour of assembly materials.
- **Loading Conditions Data.** The loading condition such as temperature cycling is parameterised. These load parameters are also NL model input parameters. Other parameters can be considered without any limitation.
- **FE Modelling and Automation of Analyses.** A parametric finite element model is developed using the characterisation data, and FE simulation runs are scripted to allow the automation of all analyses for a defined set of data points in the design space of the parameterised load. An automated run of the FE simulations is executed. FE predictions for a defined damage parameter about a failure mode and mechanisms of the power component become available.
- **Physics-Informed Datasets.** A spatial subdomain associated with the failure site of interest is defined. Extracting the FE prediction/data of interest from all analyses is scripted to enable the automation of this step. For the defined failure site and its spatial domain, the associated mesh element locations (centre coordinates) are gathered along the respective FE predictions for the damage parameter.
- **Extended Datasets and Data Labelling.** The physics-informed datasets are processed into the format of multi-variate data points

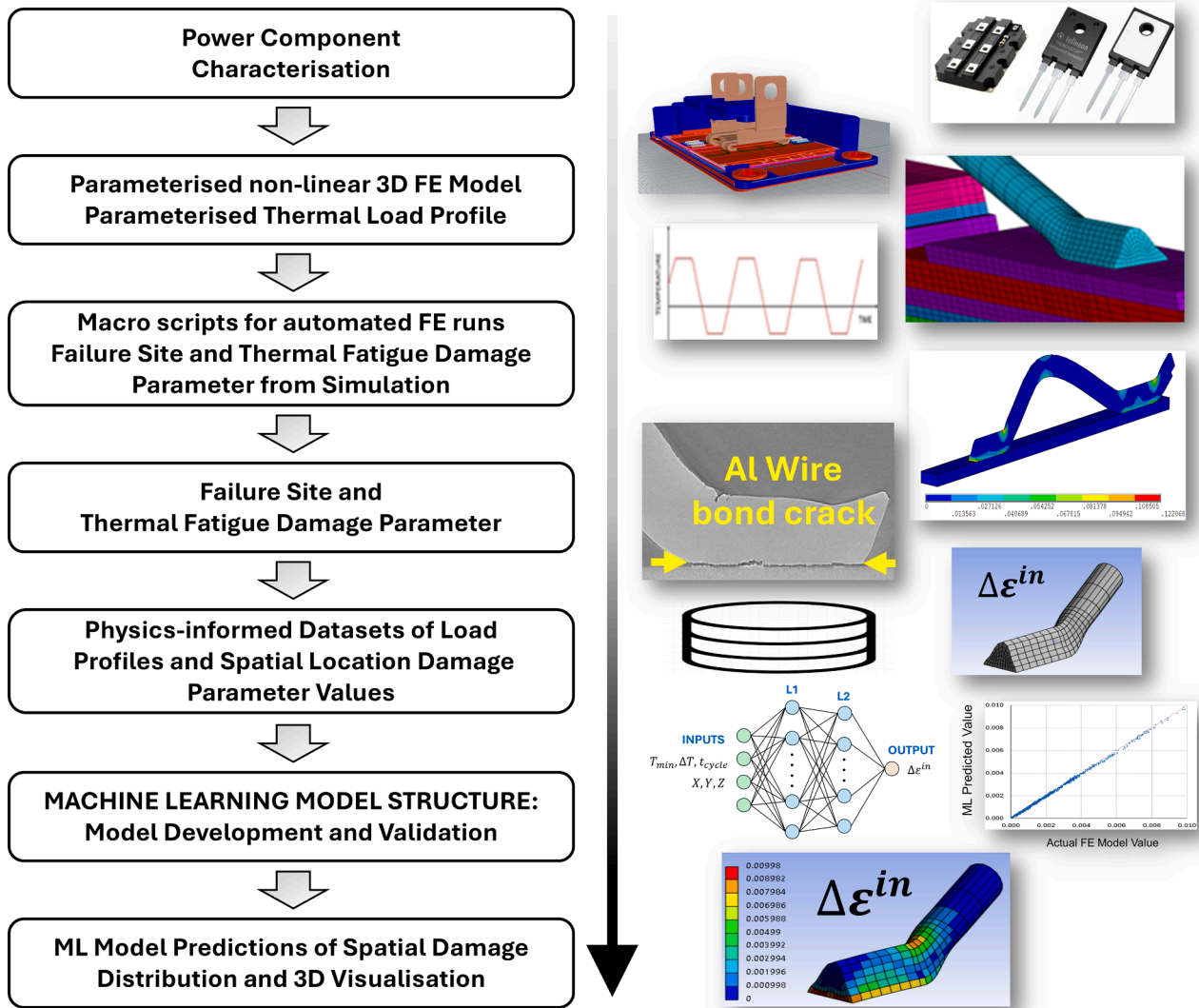


Fig. 1. A workflow diagram of the proposed damage prediction modelling methodology conceptually visualised for the problem of thermal fatigue of wire bonds in power components. Metamodelling based on physics-informed dataset generation and use, and Machine Learning model development.

(vectors), with the cyclic load parameters and the spatial location coordinates being their components. The data points are labelled with the associated damage value, as predicted by the FE simulation, for the respective load and spatial location within the defined failure site spatial domain.

- **ML Model Development.** A subset of the data (training dataset) is used to build a metamodel. Two model structures are suggested, a Decision Tree and a Neural Network, both with excellent computational and predictive power characteristics. Implement 3D visualisation graphics of the metamodel results through a spatial domain abstraction of the failure site.
- **Metamodel Validation.** Validation of the ML models is performed using the balance of the data (the validation dataset), to assess model predictive power & accuracy.

3. Power component and thermo-mechanical finite element model development

3.1. IGBT power electronic module and finite element model

The application that is used to showcase the outlined physics-informed machine learning and damage prediction modelling

methodology described in Section 2 focuses on a conventional power electronic module (PEM) and its thermal fatigue damage response under temperature cycling loads. The investigated module features an insulated-gate bipolar transistor (IGBT) power semiconductor device and a typical wire bond-based packaging architecture. Fig. 2 shows a schematic outline of a typical IGBT power module assembly. In this package, the Si devices such as the IGBT power chip and diodes are

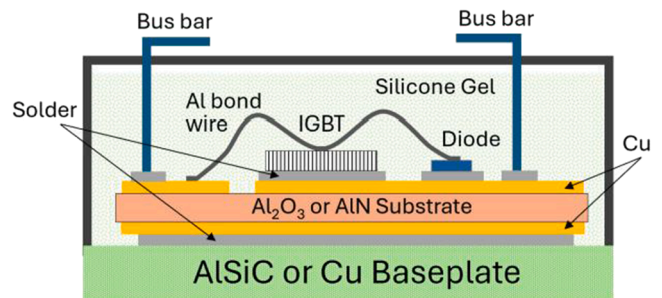


Fig. 2. A schematic outline of a typical power module package featuring an IGBT power chip and wire bond interconnection technology.

attached to a ceramic substrate that is mostly made of Alumina (Al_2O_3) or Aluminium Nitride (AlN). The substrate has double-sided copper metallization, in the form of patterned layers with thickness typically around 300 nm. The copper metallization artwork on the substrate is formed through direct thermal bonding, hence the reference to the metallized substrate as a direct bond copper (DBC) substrate. The assembly of the chip and the DBC substrate is attached to the baseplate by soldering. The baseplate, typically Cu or AlSiN, provides the structural integrity for the entire package and acts as the interface with the cold plate or heat sink which are common thermal management solutions for power modules.

The PEM investigated in this study is illustrated in Fig. 3a which shows the internal layout and the land topology of the package, in the format of a rendered CAD drawing. The external plastic casing of the module is not visualised to allow revealing the internal construction of the assembly. Eight wires per IGBT chip are realised to carry out the current, and each wire has a bond and a stitch to the Si chip, and a bond at the other end to the copper trace pattern.

The finite element modelling deploys a 3D slice of the full module, along the full length and through the full thickness of the package, so that a single wire is fully represented in the modelled domain. Fig. 3b details the 3D slice section as a CAD model and shows the finite element mesh at the local level of the wire bond foot and heel at the chip side. In addition, the materials that made the PEM are also annotated in this figure. The solder material providing the interconnection between the Si chip and the copper layer on the AlN substrate, and similarly between the DBC substrate and the AlSiC baseplate, is SnAg alloy. The thickness of the solder layers is 100 μm . In the FEA, the 96.5Sn3.5Ag solder is modelled as visco-plastic with the Anand constitutive law and model constants reported in Wang, Cheng, Becker and Wilde (2001), Cheng et al. (2000). The power module uses thick aluminium wires with a diameter of 375 μm . Due to the symmetry plane, only half of the 3D slice domain shown in Fig. 3b) is used for the FE model and simulations.

3.2. Material modelling of aluminium wire

In this study, most attention was given to the accurate material modelling of the Al wire. The reason is that the failure mode of interest discussed in this study, and to which the modelling approach is tailored as a demonstration, is the thermal fatigue cracking of the wire bond foot at the interface with the Si chip. To predict the damage in the wire bond locally at this location, the aluminium wire needs to be modelled accurately in terms of its material properties, their temperature dependency, but most importantly accounting for the plastic and creep behaviour of the aluminium using respective material behaviour constitutive laws. The material properties of the aluminium wire used in the finite element analyses are sourced from Shishido et al. (2021); ASME (2001) and are listed in Table 1.

Both the time-independent plasticity associated with kinematic hardening and the Bauschinger effect and the primary time-dependent creep behaviour of the aluminium wire are included. To achieve this, temperature-dependent constitutive equations for plastic and creep behaviour of an aluminium wire are derived using the isothermal tensile test data reported in Shishido et al. (2021).

We considered the non-linear kinematic hardening rule to simulate the plastic deformation of the aluminium wire which allows the modelling of cyclic hardening and can capture the Bauschinger effect. The nonlinear kinematic hardening model for aluminium which is developed in this work is a rate-independent version of the kinematic hardening model for the back-stress tensor α proposed by Chaboche (1989), Chaboche (1991), and obtained by superimposing three

Table 1

Properties of aluminium used in the finite element model (Shishido et al., 2021; ASME, 2001).

| Temperature ($^{\circ}\text{C}$) | -73 | 20 | 93 | 150 | 204 | 260 |
|---------------------------------------|-------|------|------|------|------|------|
| Elastic Modulus (GPa) | 73.8 | 70.3 | 66.9 | 64.8 | 61.4 | 57.2 |
| CTE ($\text{ppm}/^{\circ}\text{C}$) | 24.5 | | | | | |
| Poisson's ratio (-) | 0.345 | | | | | |

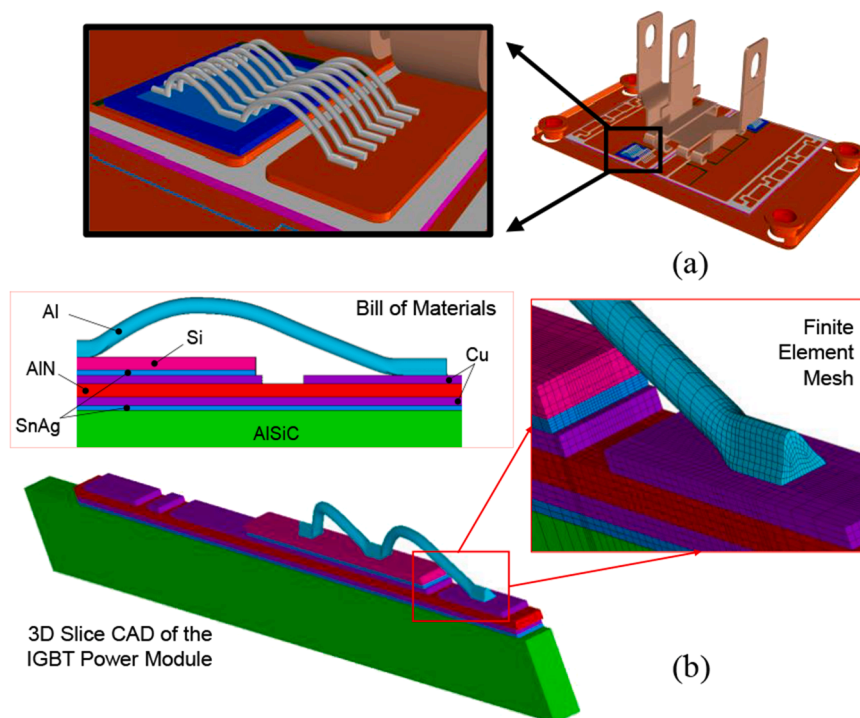


Fig. 3. (a) Topology outline of the power electronic module architecture, with a close view of the IGBT chip and wire bonds, and (b) 3D CAD slice model of the device along the full length of the module, capturing a single wire, close view of the FE mesh density at the wire bond level, and annotation of the bill of materials.

evolving kinematic back-stress tensors α_i , $i = 1, 2, 3$, as given in the following equation:

$$\alpha = \sum_{i=1}^3 \alpha_i \quad (1)$$

The evolution of each back-stress in this material model is defined with the kinematic hardening rule,

$$\dot{\alpha}_i = \frac{2}{3} C_i \dot{\epsilon}^{pl} - \gamma_i \dot{\epsilon}^{pl} \alpha_i \quad (2)$$

where C_i and γ_i are model material parameters, $\dot{\epsilon}^{pl}$ is the plastic strain rate, and $\dot{\epsilon}^{pl}$ is the magnitude of the plastic strain rate. The temperature-dependent Chaboche model material parameters C_i and γ_i for aluminium that were derived are detailed in Table 2. The plastic strain vs stress curves given with this model, at three different temperatures, are shown in Fig. 4a.

The creep behaviour of the tick aluminium wire follows the Norton-Bailey type constitutive equation for transient creep derived by Shishido et al. as part of their experimental and modelling study on tick aluminium wire (Shishido et al., 2021). The form in which this constitutive law has been reported was not suitable to be taken by most finite element codes and therefore has been modified to the form of a creep rate equation under the assumption of strain hardening under variable stress. The strain hardening creep model that is deployed, and to which the creep strain versus time data was fitted, is defined with the equation

$$\dot{\epsilon}^{cr} = C_1 \sigma^{C_2} (\epsilon^{cr})^{C_3} \quad (3)$$

where ϵ^{cr} denotes the creep strain, $\dot{\epsilon}^{cr}$ is the creep strain rate, σ is the applied stress (in unit MPa), and C_1 , C_2 and C_3 are material constants related to creep deformation. In this constitutive model, the creep strain rate dependency on the temperature is captured through the temperature-dependent definitions of the creep constants, defined as

$$\begin{aligned} C_1 &= mA^{1/m} \\ C_2 &= \frac{2.076}{m} \\ C_3 &= 1 - \frac{1}{m} \end{aligned} \quad (4)$$

where both m and A are temperature-dependent material constants (Shishido et al., 2021):

$$A(T) = 7.695 \times 10^{-4} e^{\frac{-1693}{T}} \quad (5)$$

$$\begin{aligned} m(T) &= 8.442 \times 10^{-6} (T - 273.15)^2 - 1.824 \times 10^{-3} (T - 273.15) \\ &+ 0.4054 \end{aligned} \quad (6)$$

and T is the temperature in the unit of Kelvin. In the above expressions,

the constant C_1 has the unit of $\left[\text{MPa}^{-\frac{2.076}{m}} \text{sec}^{-1} \right]$, and C_2 and C_3 are

dimensionless. The creep strain vs stress curves for aluminium wire obtained as a non-linear response under stress level of 20 MPa, at three

different temperatures, and based on the constitutive law in Eq. (3) are given in Fig. 4b.

3.3. FE simulations and fatigue damage predictions

In line with the methodology, the runs of FE thermo-mechanical simulations of the power module are implemented, in a fully automated manner, through ANSYS APDL scripting (ANSYS, 2023), where different thermal cycle load profiles are evaluated with the different simulation runs. A temperature cyclic load is defined with three parameters: (1) the low-temperature extreme of the cycle, T_{min} , (2) the temperature range ΔT of the cycle, and (3) the total duration of the temperature cycle, t_{cycle} . With this cycle-load parameterisation, the assumption of having the same temperature ramp times and dwell times in the cycle is made. This assumption is not a limitation, and separate (unequal) ramp times/rates and/or dwell times can be added and used to prescribe a less uniform temperature cycle load.

The FE model generation and load case setup in the parameterised space of the load-defining parameters is fully scripted using the ANSYS APDL command language and macro script functionality. This allows for the complete automation of simulation runs with different temperature cycle load parameters. For this problem, a single FEA transient simulation of three consecutive temperature cycles with a given profile took about 50–65 min, depending on the load cycle duration that was simulated and the associated inelastic strain rates. It was carried out using shared memory parallel with 16 processors of high-performance computing run on Intel(R) Xeon(R) processor workstation at 2.20 GHz, with 10 cores and 20 logical processors.

Different failure modes are possible for a power electronics module. From a reliability point of view, the failure of the wire bonds is of prime concern. Typically, two thermal fatigue failure modes are observed – cracking of the wire at the heel location and wire lift-off which is a result of a crack of the wire at the foot interface with the contact pad, typically on the chip side. Thermo-mechanical FE simulation results for inelastic strain or inelastic strain energy density accumulated per temperature cycle are most used as damage metrics of the assembly materials. In this investigation, the deployment of material models for the tick aluminium wire plastic and creep response to temperature cycling loads enabled the predictions of inelastic (combined plastic and creep) strain range per cycle, $\Delta \epsilon^{in}$, extracted from the 3rd simulated cycle of the transient response that ensures a stabilised hysteresis loop. This parameter is a characteristic indicator of the thermal fatigue damage induced in the aluminium wire bonds under a given load profile. The distribution and the magnitude of the $\Delta \epsilon^{in}$ in the spatial domain of the wire foot attached to the chip can inform about the reliability performance and the severity of damage and can also allow calculation of cycles to failure through the deployment of a suitable lifetime model. The local spatial distribution of the damage parameter is a critical requirement, to allow for the deployment of different lifetime prediction methodologies where the damage metric for the lifetime model may be formulated differently. Commonly, the interfacial layer is used to calculate a volume weighted average of the damage parameter which ensures a result that is mesh independent. For this reason, the finite element mesh results are processed and observed in the form of mesh element results as opposed to the more conventional nodal results.

Fig. 5a shows an example of FE simulation predictions for the thermal fatigue damage parameter in the wire bond foot domain next to the chip, in the form of an inelastic strain range per cycle $\Delta \epsilon^{in}$. Because of the deployment of separate material models for the time-independent plastic behaviour and the time-dependent creep of the aluminium wire, it is also possible to observe and evaluate the individual contributions of the plastic and creep strain ranges per cycle to the total inelastic strain range.

Fig. 5b shows the contours of the plastic strain range per cycle in the Al wire and Fig. 5c is a similar plot of the creep-related strain, both

Table 2
Chaboche kinematic hardening model parameters (temperature dependent) for Aluminium.

| Temp (°C) | σ_0 (MPa) | C_1 (MPa) | γ_1 | C_2 (MPa) | γ_2 | C_3 (MPa) | γ_3 |
|--------------|---------------------|----------------|------------|----------------|------------|----------------|------------|
| 20 | 19.94 | 8941 | 1615 | 891 | 123 | 340 | 9.9 |
| 120 | 20.99 | 7259 | 1655 | 686 | 126 | 254 | 10.2 |
| 220 | 13.16 | 4830 | 1655 | 448 | 125 | 164 | 10.2 |

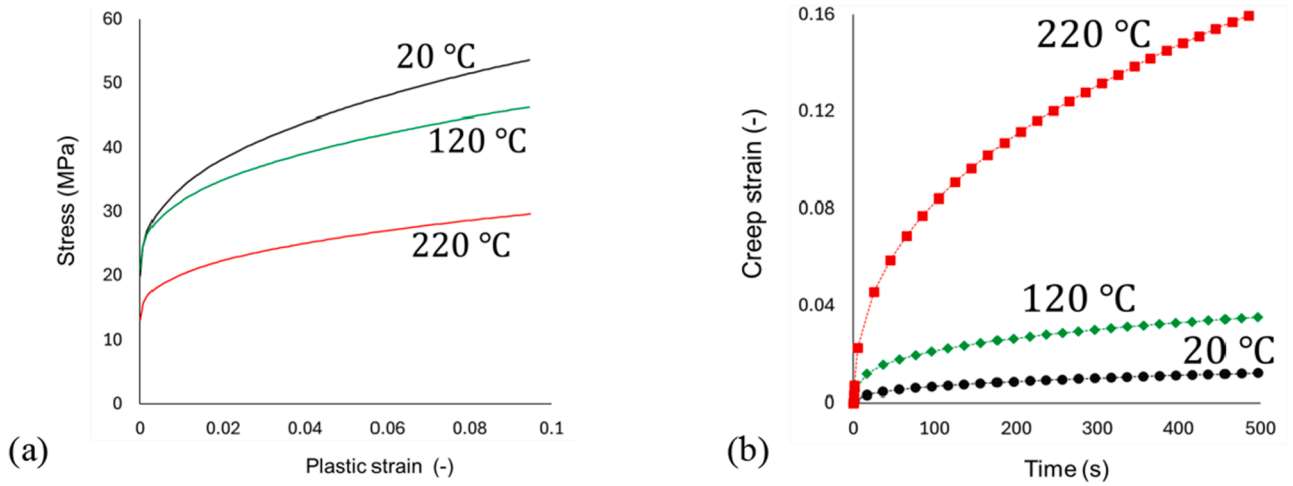


Fig. 4. Inelastic mechanistic response of Al wire at different temperatures given with the (a) Chaboche kinematic hardening model, Eq. (1)-(2) and (b) Strain hardening creep response at 20 MPa, Eq. (3).

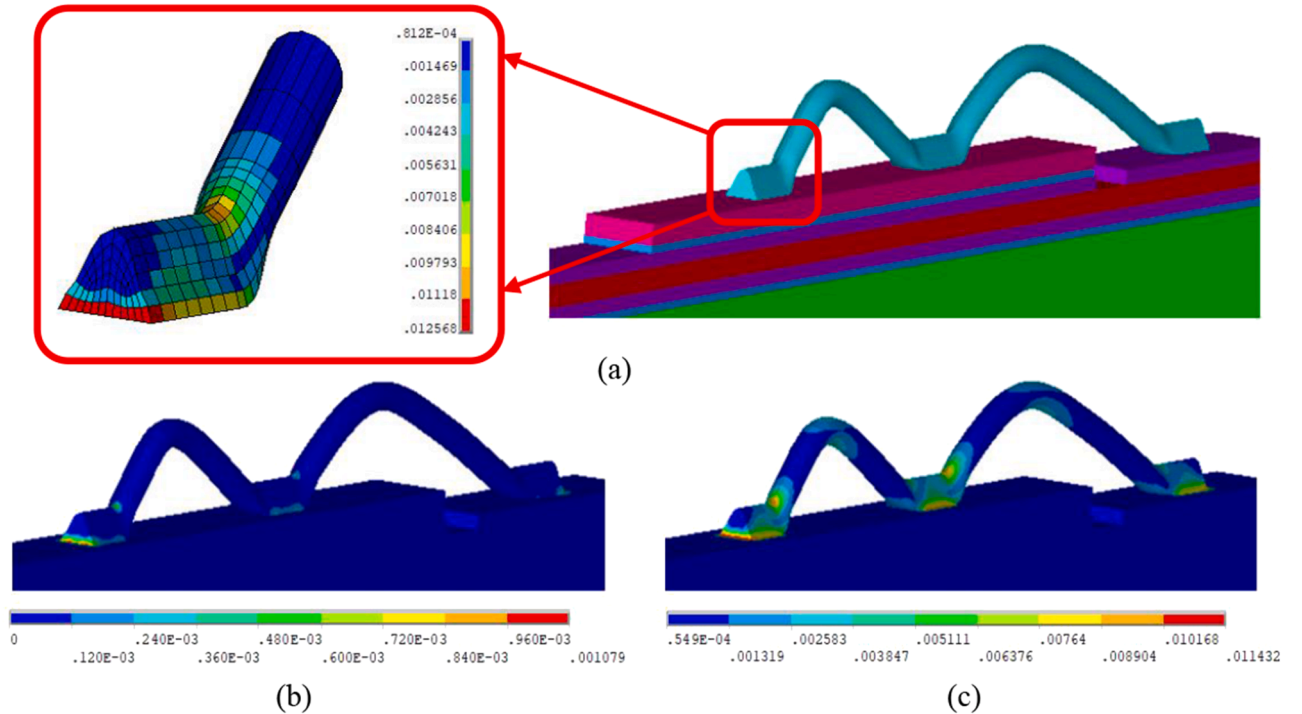


Fig. 5. Example of FE simulation predictions for the load case $T_{min} = 0^\circ\text{C}$, $\Delta T 180^\circ\text{C}$, $t_{cycle} = 3600\text{s}$. (a) Inelastic strain range per cycle (fatigue damage parameter), $\Delta\epsilon^{in}$, and its distribution in the Al wire bond foot (chip interface connection). The most critical site is the interfacial region where the crack formation is predicted. (b) Plastic strain range per cycle, $\Delta\epsilon^{pl}$, contour plots for the Al wire. (c) Creep strain range per cycle, $\Delta\epsilon^{cr}$, contour plots for the Al wire.

results are associated with the load case of $T_{min} = 0^\circ\text{C}$, $\Delta T = 180^\circ\text{C}$, $t_{cycle} = 3600\text{s}$. In this instance, creep deformation is the dominant mechanism, with the plastic strain contribution to the inelastic strain range being less than 10%. Similarly, such small and in some cases even negligible pure plastic response of the wire is found across all simulated load scenarios. This is not surprising and is explained by the very small strain rates of the passive temperature cycling load where the cycle duration is very long, in the range of 2400–3600 s. These slow temperature fluctuations favour creep and stress relaxation which result in wire deformations and associated stresses typically not exceeding the yield strength. It should be noted here that faster temperature cycles such as in power cycling will reduce the creep deformation and plasticity will feature strongly. This only emphasises the importance of choosing

relevant material models to cover all possible behaviours, so that the response of an assembly material is accurately predicted. In the remainder of the paper, only the inelastic strain range per cycle will be used.

4. Physics-informed machine learning models of damage spatial distribution

4.1. Datasets

The data required for model development using machine learning algorithms are generated with the parameterised thermo-mechanical three-dimensional finite element model detailed in Section 3, and the

automated run of 55 load-case simulations. Each analysis is a simulation of the PEM response to a particular passive temperature cyclic load defined with the three temperature profile parameters T_{min} (°C), ΔT (°C), and t_{cycle} (s). Thus, a temperature cyclic load condition for any of the load-case simulations is defined by the triplet of the defined parameters and mathematically can be expressed as a three-dimensional vector $(T_{min}, \Delta T, t_{cycle})_i$, $i = 1, m$, where in this investigation $m=55$. Here, 45 of the load profiles are used to create the dataset of physics-informed (through high fidelity non-linear FE simulation) fatigue damage data for the failure site of interest – the wire bond foot – and about the lift-off failure mode. This data is deployed to develop the machine learning models through a supervised training process and therefore is referred to as the training data following machine learning terminology. The remaining 10 load cases are used only for validation of the developed Machine Learning models, by assessing their accuracy against the respective FEA results which are taken as the ground truth.

The cycling load profiles used to generate the training dataset are defined in a structured manner over a truncated design space for the load so that the physical feasibility of the cycle definition is retained, that is the cycle parameters are within the defined range limits. The following parameter levels are deployed and visually detailed with the plots in Fig. 6:

- 5 levels (equally spaced) of T_{min} in the range 0 °C to 144 °C.
- 5 levels of ΔT (equally spaced), in the range 36 °C to 180 °C.
- 3 levels of t_{cycle} , defined as 2400s, 3000 s, and 3600s.

The remaining 10 load cases, detailed in Table 3, are not used in the training of the ML models and are only deployed to validate the developed models.

The realisation of the ML model capability for mapping the spatial damage distribution, as available in the case of finite element simulations, is achieved through the following approach. The local spatial domain of the failure site is selected first, in this instance this is the Al wire foot, extended to the heel, at the interface with the chip. The three-dimensional spatial domain is defined in geometric terms by the same FE model mesh element topology. The damage parameter spatial location values are associated with the FE mesh element centre locations for the mesh elements in the defined spatial domain of the failure site (i.e. the domain shown in Fig. 5a). Because the spatial domain is a full three-dimensional domain of the wire bond foot, X, Y and Z Cartesian system coordinates are deployed to define a spatial location.

The mesh topology of the foot has 486 mesh elements, and therefore we define 486 spatial locations with coordinates (X_j, Y_j, Z_j) , $j = 1, 2, \dots$,

486, that correspond to the geometric centres of these mesh elements.

The training dataset for building the ML models is now assembled as a combination of the thermal load-cycle data points, $(T_{min}, \Delta T, t_{cycle})_i$, $i = 1, 2, \dots, 45$ and the location datapoints, (X_j, Y_j, Z_j) , $j = 1, 2, \dots, 486$, resulting in 21,870 data points. Each data point in this extended dataset is a 6-dimensional vector $(T_{min}, \Delta T, t_{cycle}, X, Y, Z)_k$, $k = 1, 2, \dots, 21,870$. The data set is normalized over the range [0, (Falck et al., 2018)] as part of the ML development procedure. Each of these points is labelled with the respective damage value $\Delta \varepsilon^{in}$ at that location as obtained from the respective FE analysis at the location-matching mesh element. The damage values are also normalized over [0, (Falck et al., 2018)], based on the actual range found with the training dataset. The same procedure is followed with the load-cycle cases set aside to generate the datasets for ML model validation. The size of the validation dataset is 4860 data points.

4.2. Decision tree model development

Decision Tree (DT) regression is a highly effective Machine Learning algorithm capable of handling and modelling non-linear relationships and feature interactions in numerical datasets. It works by constructing a tree-like model structure to predict continuous numerical outcomes. Each pathway from the root to a leaf node corresponds to a specific decision rule, providing clarity on how predictions are generated. Instead of relying on a single regression equation, decision trees divide the data into regions based on feature value thresholds, minimising an error metric at each split. The data is divided into regions/nodes based on measuring the variance and the standard deviation.

The variance within the nodes is the spread of the target variable value within the node. A node with high variance represents that its target variables are widely spread and might be beneficial to split further. Alternatively, it is good to minimize the variance across the nodes. The higher the variance the better the split. For the dataset in this study, the decision trees produce excellent results because of the tight bound characteristics of the within-node clusters, minimizing both the variance and standard deviation without causing overfitting.

4.3. Neural network model development

The availability of labelled datasets also suits the development of regression-type Neural Network predictive models. The training dataset is used to train a regression Neural Network model structure with six inputs $(T_{min}, \Delta T, t_{cycle}, X, Y, Z)$, and a single output, $\Delta \varepsilon^{in}$. The MATLAB scientific programming environment is used to realise the NN model

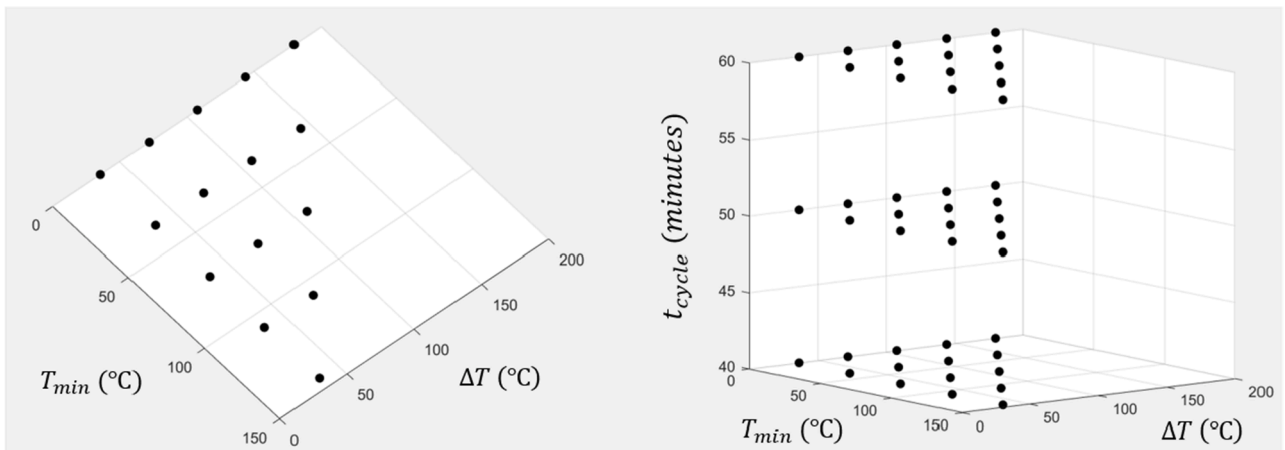


Fig. 6. Temperature load-cycle cases analysed with FE simulations to produce the physics-informed training dataset for machine learning modelling. The pair combinations of T_{min} and ΔT shown on the left side of the figure are replicated at the three levels of the t_{cycle} parameter, as illustrated on the right side, thus resulting in a total of 45 load cases.

Table 3
Definition of 10 temperature load-cycle cases used for ML model validation.

| | | Load Case Ref. Number, # | | | | | | | | | |
|------|-----------------|--------------------------|------|------|------|------|------|------|------|------|------|
| | | 1 | 2 | 3 | 4 | 5 | 6 | 7 | 8 | 9 | 10 |
| Load | T_{min} (°C) | 18 | 54 | 90 | 18 | 18 | 18 | 54 | 90 | 18 | 18 |
| | ΔT (°C) | 72 | 72 | 72 | 144 | 108 | 72 | 72 | 72 | 144 | 108 |
| | t_{cycle} (s) | 2700 | 2700 | 2700 | 2700 | 2700 | 3300 | 3300 | 3300 | 3300 | 3300 |

development, by deploying a hyperparameter optimisation procedure during the training process. A fully connected model structure with 3 hidden layers and size of (97, 193, 92), and with rectified linear unit (ReLU) activation function for the fully connected layers of the neural network model, were found to minimise the loss function most. The actual minimisation of the mean squared error (MSE), i.e. the loss function in the NN training process, was performed with the limited-memory Broyden-Fletcher-Goldfarb-Shanno quasi-Newton algorithm (L-BFGS) (Liu & Jorge Nocedal, 1989). The model structure also deploys the standardized form of the predictor data, i.e. each numeric predictor variable is centred and scaled by the corresponding variable mean and standard deviation given by the dataset parameter's values.

An important model parameter is the regularization strength of the Neural Network. To identify the optimal value, the cross-validation loss of the neural networks with the optimal layers structure is assessed with different regularization strengths. The optimum value of the regularization strength to train the final model is selected as the value that yielded the best-performing model. Here, 5-fold cross-validation is utilised and the mean squared error (MSE) for neural network regression models is used to inform on the best-performing model. The optimal value of the regularization strength that yields the best model structure is identified as 2.05E-06.

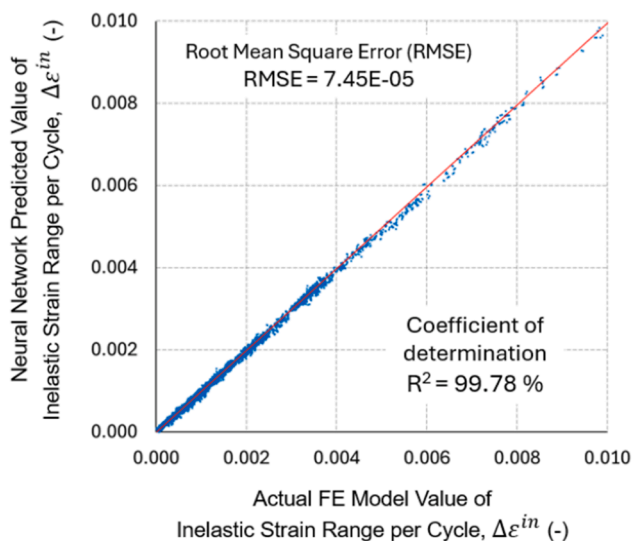
5. Results and discussions

The accuracy of the Neural Network and the Decision Tree models is evaluated using the 4860 data points in the validation dataset. The predictive power of both models is detailed in Fig. 7. These graphs show the actual FEA values of the damage parameter plotted against the predicted values obtained by the ML models. Both models are very

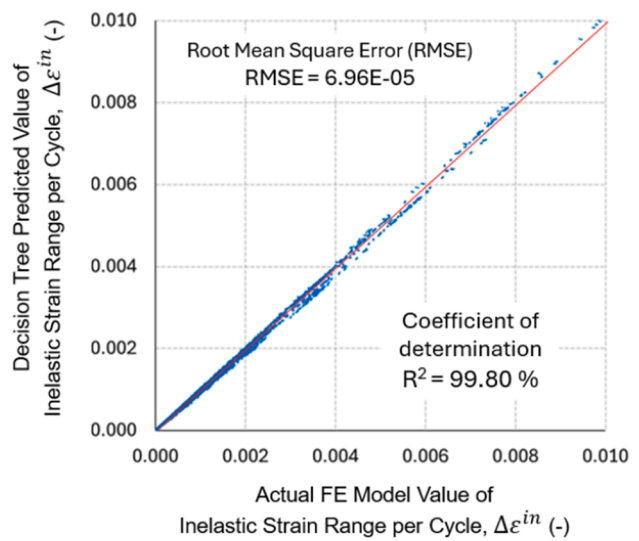
accurate and have similar performance indicated by the R-squared score values of about 99.8 %. The RSME values for both models are also listed in the figure next to the respective model plots, with the Decision Tree model showing marginally better performance.

The model accuracy indicators suggest that both the DT and the NN model have a very good predictive power, matching closely the actual FEA predictions for the parameter of interest ($\Delta \epsilon^{in}$). The accuracy is expected to improve further if the size of the training data is increased. The damage parameter values, dominated by the creep response of the aluminium wire, are dependent on and sensitive to the temperature regime of the cycle and the time duration in a non-linear manner. More importantly, the damage response $\Delta \epsilon^{in}$ values at different spatial locations defined by the mesh topology of the wire foot domain have very different magnitudes, yet such highly non-linear spatial distribution is accurately captured with the two investigated models. Even more, the approach is scalable, particularly in expanding the number of spatial locations for which the ML model is designed to provide predictions. This offers some interesting opportunities for reasonably detailed and informative mapping of physics-based parameter results in 3-dimensional subdomains of a physical system.

As part of this methodology, the visualisation of the ML model results is needed through mapping the predictions back onto the actual wire foot spatial domain. To do that, the ML model needs to predict the $\Delta \epsilon^{in}$ values for a set of data points that cover spatial locations of the domain of interest, for a given load-cycle profile. With this data available, a visual mapping using a suitable visualisation software tool can be realised. In this work the visualisation of the ML results is done using Ansys Workbench and an add-on extension tool – CSV Plot - for mapping external results on a predefined mesh topology over a spatial domain. CSV Plot is a post-processing tool, developed by EDR Medeso, that en-



(a)



(b)

Fig. 7. ML model predicted values vs. ground truth FEA values of the inelastic strain range per cycle values $\Delta \epsilon^{in}$ obtained for the validation dataset (4860 data points). Each data point in the validation dataset represents a cyclic thermal load condition (T_{min} , ΔT , Δt_{cycle}) and a 3-dimensional (X, Y, Z) spatial location of the wire bond foot spatial domain: (a) ML model of Neural Network and (b) ML model of Decision Tree.

ables the creation of custom nodal or element contour plots from CSV file (CSV, Tool). Therefore, the visualisation requires first to have the wire foot local spatial domain topology and the corresponding mesh elements developed or imported in the Ansys Workbench environment, so that the absolute spatial position of the domain matches the one assumed with the ML model training. The ML predictions are then organised as a CSV file where each line contains a spatial point X, Y and Z coordinates, and the visualised parameter value at that point ($\Delta\epsilon^{in}$).

To demonstrate the deployment of the two ML models, we explicitly run the Neural Network, and the Decision Tree models with the input data that define two of the validation load cases, numbers #4 and #8 in Table 3. The number of input data points for each case is given by the number of spatial locations associated with the 3D visualisation mesh topology of the wire bond foot. The data point parameters associated with the temperature load definition remain the same as per the respective validation case.

Fig. 8 demonstrates the FE, DT and NN model predictions for the $\Delta\epsilon^{in}$ at the failure site of interest, for the validation load case #4 (the load-cycle profile, defined with $T_{min} = 18^\circ\text{C}$, $\Delta T = 144^\circ\text{C}$ and $\Delta t_{cycle} = 3,300$ s). Here, the 3D visualisation mesh topology deploys the same FE model mesh topology to allow for the direct comparison and benchmarking of the spatial predictive capability of the ML models versus the FE model results. This means that the spatial coordinate components of the input vectors for the ML models use the X-Y-Z coordinates of the mesh elements centres as in the FE model, within the defined wire bond foot 3D domain. There is no restriction to utilising a different mesh topology for the visualisation over the same geometric domain and to run the ML models with these spatial locations to obtain the predictions for damage. In Fig. 8(b), the contour plot of $\Delta\epsilon^{in}$ is the FE result obtained from a non-linear transient finite element simulation undertaken using ANSYS APDL (note: results taken into the ANSYS Workbench using CSV, Tool for visualisation purposes only). All three plots use the same legend scale to allow for the visual comparison of the results. The DT and the NN modelling predictions match the FE contour plot scale bands almost identically across all mesh element locations. The difference between the peak value obtained with the Neural Network differs by 0.5 % when

compared with the FE model peak value prediction, and similarly, the difference in the maximum value predicted with the Decision Tree and the FE models is 0.9 %.

In Fig 9, a similar comparative analysis is detailed but this time using the validation load case #8, which is given with the load-cycle profile $T_{min} = 90^\circ\text{C}$, $\Delta T = 72^\circ\text{C}$ and $\Delta t_{cycle} = 2,700$ s. These results, taken in the context of the results in Fig. 8 for a different load case scenario, confirm that changes in the temperature profile load do not affect notably the spatial distribution of the damage parameter within the failure site domain under investigation. This is not surprising, because the deformation dynamics of the wire during temperature cycling is driven by the same factors that are present with any load case, that is the global CTE mismatch between the assembly materials (here particularly at the local level between the Si chip and Al wire) and the overall PEM topology and layout, as well as the given geometric dimensions of the internals. The critical locations where crack would be anticipated to form first and propagate are at the wire bond foot interface with the chip and the heel locations. Failures at these locations are widely reported so these modelling results agree and confirm that. The capability of the two ML models to deliver predictions for the damage parameter with FE-matching accuracy, including in terms of the highly non-linear spatial distribution of the predictions, means that outputs from the ML models can enable the calculation of damage values that lifetime models required, thus supporting reliability predictions for the wire bond failure. For the load case detailed in Fig. 9, the NN and the DT model predictions of the maximum absolute value of $\Delta\epsilon^{in}$ are also very accurate, deviating only by 1.3 % and 0.3 % from the FE model prediction, respectively.

The mean value of the relative error of the predicted maximum inelastic strain range per cycle $\Delta\epsilon^{in}$ for the ten validation load cases in Table 3 is 2.18 % for the Decision Tree model and 1.65 % for the Neural Network model, and the standard deviations of the relative error are 2.2 % and 0.7 %, respectively.

The ability to achieve good model accuracy is important in the context of the rationale for carrying out this investigation. From a practical point of view, assessing the reliability performance of the PEM,

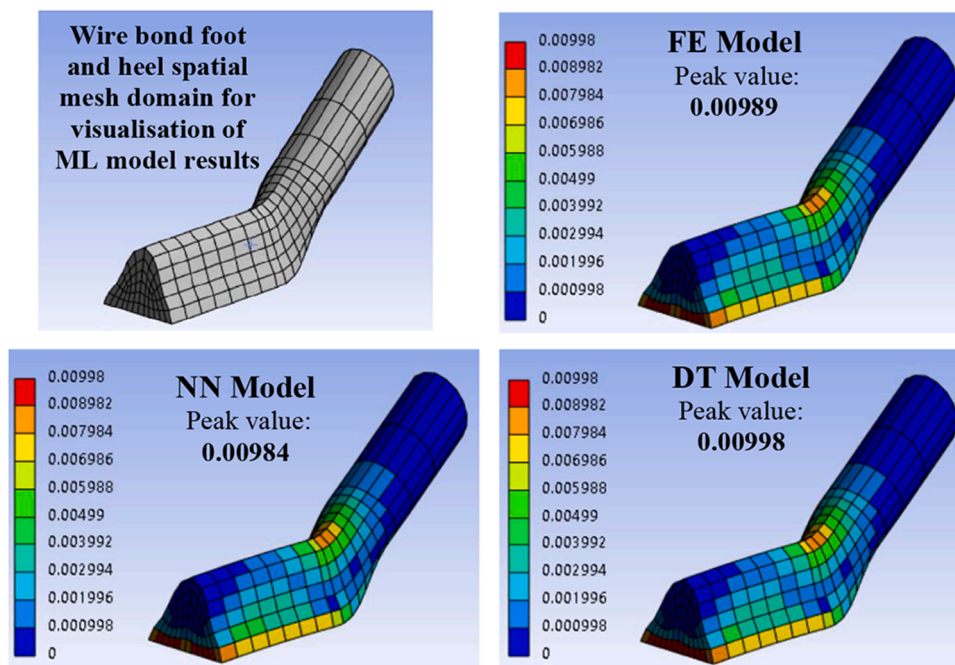


Fig. 8. (a) The Al wire bond foot at the interface with Si chip spatial domain for model predictions of damage and associated mesh topology for visualisation given with the mesh resolution set in the FE model. Damage parameter ($\Delta\epsilon^{in}$) prediction provided by (b) detailed non-linear finite element analysis, (c) Neural Network model, and (d) Decision Tree model. Results are for the validation case #4 defined with temperature cycle load $T_{min} = 18^\circ\text{C}$, $\Delta T = 144^\circ\text{C}$ and $\Delta t_{cycle} = 3,300$ s, and spatial locations of data points given with mesh element centre coordinates (X,Y,Z) of 3D visualisation mesh topology.

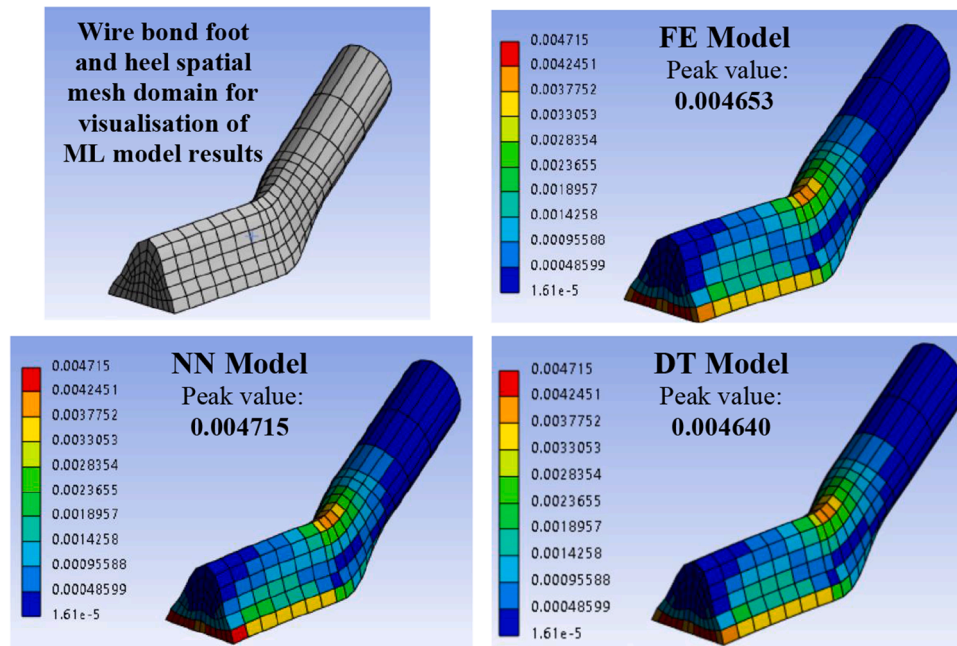


Fig. 9. (a) The Al wire bond foot at the interface with Si chip spatial domain for model predictions of damage and associated mesh topology for visualisation given with the mesh resolution set in the FE model. Damage parameter ($\Delta\epsilon^{in}$) prediction provided by (b) detailed non-linear finite element analysis, (c) Neural Network model, and (d) Decision Tree model. Results are for the validation case #8 defined with temperature cycle load $T_{min} = 90^{\circ}\text{C}$, $\Delta T = 72^{\circ}\text{C}$ and $\Delta t_{cycle} = 2700$ s, and spatial locations of data points given with mesh element centre coordinates (X, Y, Z) of 3D visualisation mesh topology.

e.g. wire bond failure, through model predictions of damage and/or using conventional fatigue lifetime models (Coffin-Manson, Paris, etc.) need only the results of the damage metric at the failure site only, not across the entire structural domain. Yet, with the FE approach a full-order FE model is needed of the entire structure to capture the material interactions, all input data for the CAD model, material properties and their constitutive laws for plasticity and/or creep, and a transient simulation of the cyclic load, to allow ultimately for a subset of results that are needed to become available for the damage/lifetime predictions.

With the proposed approach, such output can be achieved with acceptable accuracy, by providing suitable in size training data. A few advantages can be pointed out. Once developed, the ML models allow for design exploration in the load-cycle parameters. From a PEM end-user point of view, this is predominantly the parametric space of the thermal load definition, allowing them to assess the PEM reliability performance under different load conditions as dictated by the different applications for which these modules are intended. With the proposed modelling technology, end-users can do such evaluation without the need to fully characterise the PEM. Once constructed, the ML models can be operated and used as real-time models – they provide predictions instantaneously. In contrast, non-linear FE simulation run times can take minutes or hours.

6. Conclusions

A novel modelling approach for ML-driven metamodel development has been formulated and demonstrated for the problem of predicting the thermal fatigue damage of electronics assembly materials. The computational framework extends current deployments of metamodels and machine learning models from the application load domain to the spatial physical domain. It has the potential to handle temporal predictions in a similar manner. It takes advantage of the capability and robustness of ML to model large datasets of highly non-linear data. The proposed methodology has been successfully validated and demonstrated for a case study on the thermal fatigue of wire bonds in power electronics modules.

The main attributes of the developed modelling approach and the resulting metamodels that make this work novel can be summarised as follows:

- Deployment of synthetically generated physics-informed physical parameter data. This was achieved by high-fidelity finite-element simulations used to predict accurately the thermal fatigue degradation and failure of electronics assembly materials. This was assured by deploying very accurate and experimentally informed non-linear material behaviour constitutive laws.
- Proposed metamodels have accuracy similar to the FE models. They allow for the spatial mapping and three-dimensional visualisation of the distribution of the predicted damage parameter onto a local (failure) site of the physical domain, in a similar fashion as FE simulations.
- Deployment of highly non-linear machine learning regression metamodel structures and model parameters optimisation step to ensure the optimal model performance in terms of prediction accuracy are identified.

The advantage of the proposed modelling methodology is that no data about the semiconductor package is required to run these models, and the runtime of the analysis is only a fraction of the time that the FE simulation takes. The proposed models can be generated by the electronics component manufacturer and provided to the end-users along with the respective technical datasheet. The authors regard this as a significant contribution because it allows for the component IP protection while enabling the end-users to assess the reliability performance of the part under the loads and conditions of their application in a time and cost-efficient manner. For the end-users this also removes the requirements for deploying complex characterisation and physical tests, and for specialised software tools and modelling skill sets.

CRedit authorship contribution statement

Stoyan Stoyanov: Writing – original draft, Visualization, Validation, Supervision, Software, Resources, Project administration, Methodology,

Investigation, Funding acquisition, Formal analysis, Data curation, Conceptualization. **Razia Sulthana:** Writing – original draft, Validation, Software, Investigation, Formal analysis. **Tim Tilford:** Writing – review & editing, Visualization, Validation, Supervision, Software, Resources. **Xiaotian Zhang:** Writing – review & editing, Resources, Methodology. **Yihua Hu:** Writing – review & editing, Supervision, Resources, Project administration, Investigation, Funding acquisition, Data curation, Conceptualization. **Xingyu Yang:** Writing – original draft, Validation, Resources, Investigation, Data curation. **Yaochun Shen:** Writing – review & editing, Supervision, Resources, Project administration, Funding acquisition, Data curation, Conceptualization. **Yangang Wang:** Writing – review & editing, Resources, Funding acquisition, Data curation.

Declaration of competing interest

The authors declare that they have no known competing financial interests or personal relationships that could have appeared to influence the work reported in this paper.

Acknowledgements

This work was supported by the Engineering and Physical Sciences Research Council (EPSRC), U.K., through project grants EP/W006642/1, EP/W006405/1, EP/W006308/1, and partly supported through project grant EP/X024377/1. The authors would like to thank the industrial partner Dynex Semiconductor Ltd. for their contributions and technical guidance, and for providing power electronics module samples and characterisation data.

Data availability

Data will be made available on request.

References

- ANSYS (2023). Mechanical APDL 2023 R1 - Theory Reference, <https://www.ansys.com/ASME>. (2001). *Code for pressure piping, standard ASME B31.1-2001* (p. 223). Power Piping.
- Busca, C., Teodorescu, R., Blaabjerg, F., Munk-Nielsen, S., Helle, L., Abeyasekera, T., & Rodríguez, P. (2011). An overview of the reliability prediction related aspects of high power IGBTs in wind power applications. *Microelectronics Reliability*, 51(9–11), 1903–1907.
- Chaboche, J. L. (1989). Constitutive equations for cyclic plasticity and cyclic viscoplasticity. *International Journal of Plasticity*, 5, 247–302.
- Chaboche, J. L. (1991). On some modifications of kinematic hardening to improve the description of ratchetting effects. *International Journal of Plasticity*, 7, 661–678.
- Cheng, Z. N., Wang, G. Z., Chen, L., Wilde, J., & Becker, K. (2000). Viscoplastic Anand model for solder alloys and its application. *Soldering & Surface Mount Technology*, 12(2), 31–36.
- CSV Tool, EDR Medeso, <https://catalog.ansys.com/product/668dc911ae7482560e8250d0/csv-plot>.
- Dudek, R., et al. (2020). Reliability modelling for different wire bonding technologies based on FEA and nano-indentation. In *Proceedings of the 8th Electronics System-Integration Technology Conference* (pp. 1–7). Tønsberg, Norway. <https://ieeexplore.ieee.org/document/9229761>.
- Falck, J., Felgemacher, C., Rojko, A., Liserre, M., & Zacharias, P. (2018). Reliability of power electronic systems: An industry perspective. *IEEE Industrial Electronics Magazine*, 12(2), 24–35.
- Gabriel, O. E., & Huitink, D. R. (2023). Failure mechanisms driven reliability models for power electronics: A review. *Journal of Electronic Packaging*, 145(2), Article 020801.
- Gonzalez, J. O., et al. (2016). Enabling high reliability power modules: A multidisciplinary task. *Proceedings of the International Symposium on 3D Power Electronics Integration and Manufacturing* (pp. 1–5). Raleigh, NC, USA. <https://ieeexplore.ieee.org/document/7570567>.
- Grams, A., Prewitz, T., Wittler, O., Schmitz, S., Middendorf, A., & Lang, K.-D. (2014). Modelling the lifetime of aluminium heavy wire bond joints with a crack propagation law. *Proceedings of the 15th International Conference on Thermal, Mechanical and Multi-Physics Simulation and Experiments in Microelectronics and Microsystems (EuroSimE)* (pp. 1–6). Ghent, Belgium. <https://ieeexplore.ieee.org/document/6813828>.
- Hassan, S., Rajaguru, P., Stoyanov, S., Bailey, C., & Timothy Tilford, T. (2024). Coupled thermal-mechanical analysis of power electronic modules with finite element method and parametric model order reduction. *Power Electronic Devices and Components*, 8, Article 100063.
- Huang, Q., Peng, C., Ellen, S. F.-M., Zhu, W., & Wang, L. (2021). A finite element analysis on the reliability of heavy bonding wire for high-power IGBT module. *IEEE Transactions on Components, Packaging and Manufacturing Technology*, 11(2), 212–221.
- Ji, B., Song, X., Sciberras, E., Cao, W., Hu, Y., & Pickert, V. (2015). Multiobjective design optimization of IGBT power modules considering power cycling and thermal cycling. *IEEE Transactions on Power Electronics*, 30(5), 2493–2504.
- Li, Q., et al. (2023). Review of the failure mechanism and methodologies of IGBT bonding wire. *IEEE Transactions on Components, Packaging and Manufacturing Technology*, 13(7), 1045–1057.
- Liu, D. C., & Jorge Nocedal, J. (1989). On the limited memory BFGS method for large scale optimization. *Mathematical Programming*, 45(1), 503–528.
- Ma, K., Wang, H., & Blaabjerg, F. (2016). New approaches to reliability assessment: Using physics-of-failure for prediction and design in power electronics systems. *IEEE Power Electronics Magazine*, 3(4), 28–41.
- Rajaguru, P., Lu, H., & Bailey, C. (2019). Time integration damage model for Sn3.5Ag solder interconnect in Power Electronic Module. *IEEE Transactions on Device and Materials Reliability*, 19(1), 140–148.
- Rajaguru, P., Stoyanov, S., Lu, H., & Bailey, C. (2013). Application of Kriging and radial basis function for reliability optimization in power modules. *Journal of Electronic Packaging*, 135(2), Article 021009.
- Shishido, N., Hayama, Y., Morooka, W., Hagihara, S., & Miyazaki, N. (2019). Application of nonlinear fracture mechanics parameter to predicting wire-liftoff lifetime of Power Module at elevated temperatures. *IEEE Journal of Emerging and Selected Topics in Power Electronics*, 7(3), 1604–1614.
- Shishido, N., Setoguchi, Y., Kumagai, Y., Koganemaru, M., Ikeda, T., Hayama, Y., & Miyazaki, N. (2021). Characterization of plastic and creep behavior in thick aluminium wire for power modules. *Microelectronics Reliability*, 123, Article 114185.
- Stoyanov, S., Tilford, T., Shen, Y., & Hu, Y. (2024). Reliability meta-modelling of power components. In *Proceedings of the 47th International Spring Seminar on Electronics Technology (ISSE)* (pp. 1–7). Prague, Czech Republic. <https://ieeexplore.ieee.org/document/10604175>.
- Tauscher, M., Merk, T., Adsule, A., Linnemann, A., & Wilde, J. (2023). Surrogate modeling for creep strain-based fatigue prediction of a Ball Grid Array component. *ASME Journal of Electronic Packaging*, 146(1), Article 011003.
- Wang, H., & Blaabjerg, F. (2021). Power electronics reliability: State of the art and outlook. *IEEE Journal of Emerging and Selected Topics in Power Electronics*, 9(6), 6476–6493.
- Wang, G. Z., Cheng, Z. N., Becker, K., & Wilde, J. (2001). Applying Anand model to represent the viscoplastic deformation behavior of solder alloys. *ASME Journal of Electronic Packaging*, 123(3), 247–253.
- Yang, Y., Dorn-Gomba, L., Rodriguez, R., Mak, C., & Emadi, A. (2020). Automotive power module packaging: Current status and future trends. *IEEE Access: Practical Innovations, Open Solutions*, 8, 160126–160144.
- Yang, L., Agyakwa, P. A., & Johnson, C. M. (2014). Calibration of a novel microstructural damage model for wire bonds. *IEEE Transactions on Device and Materials Reliability*, 14(4), 989–994.